Automatic Matching of Cartridge Case Impressions

Joseph Zemmels
Iowa State University

Susan VanderPlas
University of Nebraska - Lincoln

Heike Hofmann
Iowa State University

Abstract

Forensic examinations attempt to solve the binary classification problem of whether two pieces of evidence originated from the same source. A cartridge case found at a crime scene may be compared to a cartridge case fired from a suspect's firearm. Historically, forensic examiners relied on high-powered comparison microscopes, case facts, and their own experience to arrive at a source conclusion. Recently, algorithms that provide an automatic and objective measure of similarity of the evidence have become more prevalent. We introduce a cartridge case comparison algorithm that encompasseses preprocessing, feature extraction, and similarity scoring. We use a train/test split on a data set of 500 cartridge case scans to fit and validate a random forest model. We demonstrate that this random forest model yields improved accuracy compared to predominant algorithms. Finally, we use the random forest model to calculate score-based likelihood ratios that estimate the probative value of the evidence.

Keywords: forensics, forensic statistics, pattern recognition, firearms and toolmarks, R.

---

1. Introduction

Introduce the problem here. Explain what a cartridge case is. Explain breech face impressions.

The "ground-truth" of a forensic comparison is a binary classification problem. Briefly reference how comparisons are done by examiners currently. Keep focus on firearm and toolmark evidence.

Critics of traditional firearm and toolmark comparisons cite a lack of foundational validity (NAS 2009, PCAST 2016). National Research Council (2009); PCAST (2016) Discuss what PCAST means by foundational validity and how firearm and toolmark evidence falls short according to NAS & PCAST. Recent studies of examiner proficiency estimate error rates to be low - between % and % according to [Baldwin]. Nonetheless, [NAS] and [PCAST] pushed for the development of "objective image processing algorithms to. . . .[quote PCAST here. . .]." An automatic comparison algorithm could be used as part of an examination to supplement or inform an examiner's opinion [cite Swofford taxonomy paper here]. Swofford and Champod (2021)

2. Previous Work

Discuss current state of affairs for algorithmic F&T comparisons.

Cite Hare et al. Hare et al. (2017) as a parallel paper to this one applied to bullet data.

Cite Xiao Hui's project.

Cite CMC method as predominant method. don't forget about cmcR :) Broadly summarize cell-based comparison procedure and CMC method logic. Also reference Zhang et al. (2020) DBSCAN paper Ester et al. (1996) here. XXX I don't know what you mean by Zhang et al 2020

Discuss limitations of current cartridge case comparison algorithms. Currently, there is no rigorous procedure for comparing different algorithms. This includes selecting optimal parameters for a specific algorithm. In this work, we introduce a novel validation procedure to learn and validate optimal parameters using a cross-validation procedure.

We introduce a novel set of features to measure the similarity between two cartridge cases. using these features, we train and test a random forest model. We show that this random forest model improves upon the error rate of predominant automatic comparison algorithms. Additionally, we demonstrate how the random forest model can be used to calculate score-based likelihood ratios.

3. Cartridge Case Data

Discuss Baldwin study here. Baldwin et al. (2014) Point out that it was the only appropriately-designed study according to PCAST. Types of cartridge cases, firearms. Design of the experiment (known and questioned samples).

Details of scanning procedure using Cadre 3D-TopMatch High Capacity Scanner. Describe x3p file format and surface matrices.

4. Methods

We now discuss the methods behind the Automatic Cartridge Evidence Scoring (ACES)

algorithm. We divide the Methods into three broad categories:

1. **Preprocessing:** prepare cartridge case scans for comparison

2. **Comparing:** compare two cartridge cases and compute similarity features

3. **Scoring:** measure the similarity between the two cartridge cases using a trained classifier

The following sections detail each of these steps.

4.1. Preprocessing

We first use the open-source FiX3P web application cite Talen Fisher to manually annotate the breech face impression region. An example of a manually-annotated cartridge case scan is shown in Figure 1. The FiX3P software includes functionality to "paint" the surface of a cartridge case using a computer cursor and save the painted regions to a *mask.* A mask is a 2D array of hexidecimal color values of the same dimension as its associated surface matrix. When initialized, every element of a mask is a shade of brown (#cd7f32) by default. Any elements that are painted-over by the user will be replaced with the user's selected color value. In Figure 1, the breech face impression region was manually annotated using a shade of red (#ff0000).
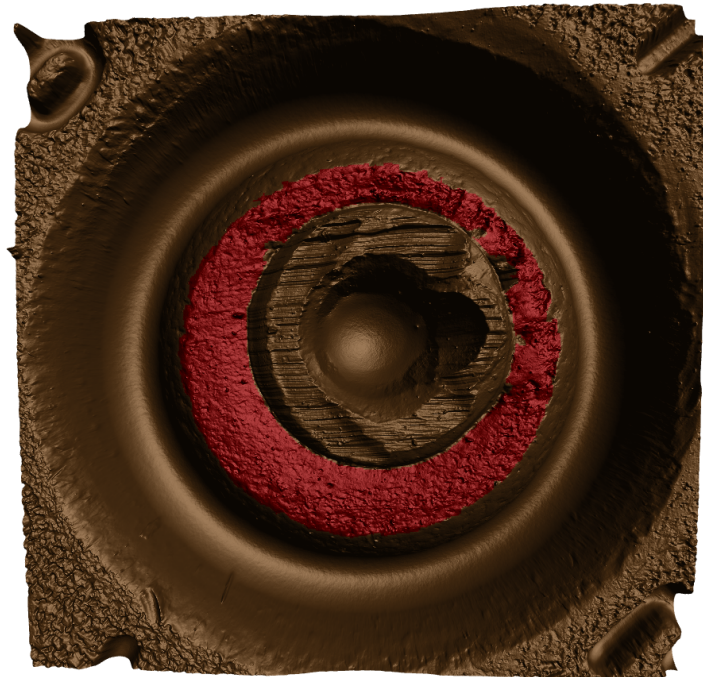

Figure 1: A cartridge case surface is manually annotated in red using the FiX3P software. The annotated region of interest contains breech face impressions.

Once read into an R environment, we use sequence of functions available in the packages [x3ptools] Hofmann et al. (2022) and [cmcR] Zemmels et al. (2022) to preprocess the raw scans. Figure 2 shows the effect that each function has on the scan

surface values. Gray pixels in each plot represent missing values in the surface matrix. The `x3p_delete` function removes values in the scan based on the associated mask. Next, the `preProcess_removeTrend` function subtracts a fitted conditional median plane from the surface values to "level-out" any global tilt in the scan. The `preProcess_gaussFilter()` function applies a bandpass Gaussian filter to remove small-scale noise and other large-scale structure, which better highlights the medium-scale breech face impressions. Finally, the `preProcess_erode()` function applies the morphological operation of erosion on the edge of the non-missing surface values [cite erosion reference]. This has the effect of shaving-off values on the interior and exterior edge of the surface, which are often extreme "roll-off" values that unduly affect the comparing stage if not removed. The final result is a cartridge case surface matrix with emphasized breech face impressions.
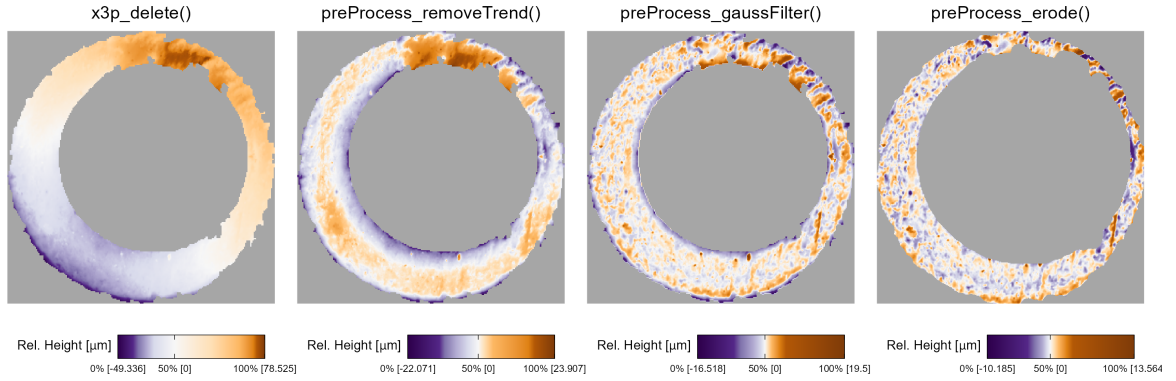

Figure 2: We apply a sequence of preprocessing functions to each scan. Each preprocessing step further emphasizes the breech face impressions in the scan.

Next, we compute a set of similarity features for two preprocessed cartridge case scans.

4.2. Comparing

In this section, we introduce a set of similarity features for two cartridge case scans. We calculate features at two scales: between two whole scans and between individual cells similar to the CMC method [cite]. Analogous to how a forensic examiner uses a comparison microscope with different magnification levels, this allows us to assess the similarity between two scans at the macro and micro levels.

Notational Conventions

First, we introduce notation that will be used to define the features. Let A and B denote two surfaces matrices that we wish to compare. For simplicity, we assume that $A, B \in \mathbb{R}^{k \times k}$ for $t > 0$.[1] We use lowercase letters and subscripts to denote a particular value of a matrix: a_{ij} is the value in the ith row and jth column, starting from the

---

[1]This assumption of equally-sized, square matrices is easily enforced by padding the matrices with additional missing values. Due to the presence of (structurally) missing values around the breech face impression region, additional padding does not interfere with the structure of the scan.

top-left corner, of matrix A. Throughout this section, we will use the two known-match cartridge cases in Figure 3 as exemplar matrices A and B.

To accommodate structurally-missing values, we adapt standard matrix algebra as follows: if an element of either matrix A or B is missing, then any element-wise operation including this element is also missing, otherwise standard matrix algebra holds. For example, the addition operator is defined as:

$$A \oplus_{NA} B = (a_{ij} \oplus_{NA} b_{ij})_{1 \leq i,j \leq k} = \begin{cases} a_{ij} + b_{ij} & \text{if both } a_{ij} \text{ and } b_{ij} \text{ are numbers} \\ NA & \text{otherwise} \end{cases}$$

Other element-wise operations such as $\ominus_{NA}$ are defined similarly. For readability, we will use standard operator notation $+, -, >, <, \dots$ and assume the extended operations as defined above.
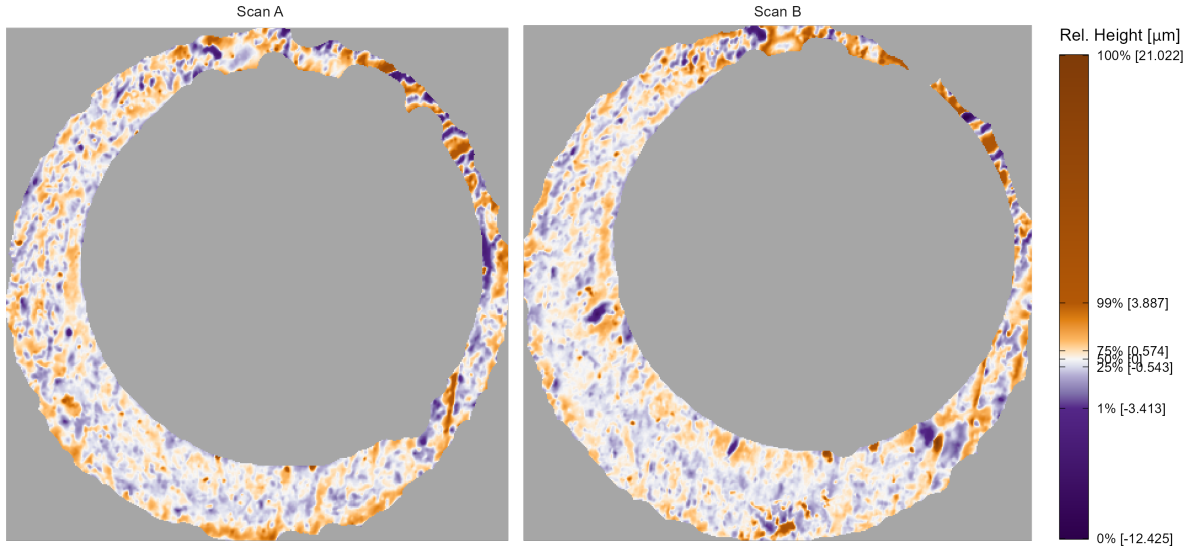

Figure 3: A matching pair of processed cartridge case scans. We measure the similarity between these cartridge cases using the distinguishable breech face impressions on their surfaces.

Registration Estimation

A critical step in comparing A and B is to find a transformation of B such that it aligns best to A (or vice versa). In image processing, this is called *image registration*. Noting that A and B are essentially grayscale images, we rely on a standard image registration technique [cite Brown, 1992].

In our application, this transformation is composed of a discrete translation by $(m, n) \in \mathbb{Z}^2$ and rotation by $\theta \in [-180°, 180°]$. Under this transformation, the index i, j maps to a new index i^*, j^* by:

$$\begin{pmatrix} j^* \\ i^* \end{pmatrix} = \begin{pmatrix} n \\ m \end{pmatrix} + \begin{pmatrix} \cos(\theta) & -\sin(\theta) \\ \sin(\theta) & \cos(\theta) \end{pmatrix} \begin{pmatrix} j \\ i \end{pmatrix}.$$

The value b_{ij} now occupies the index i^*, j^*. In practice, we use *nearest-neighbor interpolation* meaning i^* and j^* are rounded to the nearest integer [cite a nearest-neighbor reference].

To determine the optimal registration, we calculate the *cross-correlation function* (CCF) between A and B, which measures the similarity between A and B for every possible translation of B. Denoted $(A \star B)$, the CCF between A and B is a 2D array of dimension $2k - 1 \times 2k - 1$ with the m, n-th element given by:

$$(a \star b)_{mn} = \sum_{i=1}^{k} \sum_{j=1}^{k} a_{mn} \cdot b_{i+m,j+n}$$

where $1 \leq m, n \leq 2k - 1$. The value $(a \star b)_{mn}$ quantifies the similarity between A and B after B is translated m elements horizontally and n elements vertically. The CCF is often normalized between -1 and 1 for interpretability.

For large matrices, the above definition of the CCF is computationally taxing. The Cross-Correlation Theorem provides an equivalent expression for the CCF:

$$(A \star B) = \mathcal{F}^{-1}\left(\overline{\mathcal{F}(A)} \odot \mathcal{F}(B) \right)$$

where $\mathcal{F}$ and $\mathcal{F}^{-1}$ are the discrete Fourier and inverse discrete Fourier transforms, respectively, $\overline{\mathcal{F}(A)}$ is the complex conjugate, and $\odot$ is an element-wise (Hadamard) product [cite Brigham, 1988]. We trade the moving sum computation from the previous CCF expression for two forward Fourier transforms, an element-wise product, and an inverse Fourier transform. The Fast Fourier Transform (FFT) algorithm reduces the computational load considerably [cite Tukey].

Using the CCF as an objective function, we estimate the registration by calculating the maximum CCF value across a range of rotations of matrix B. Let B_θ denote B rotated by an angle $\theta \in [-180°, 180°]$ and $b_{\theta_{mn}}$ the m, n-th element of B_θ. Then the estimated registration (m^*, n^*, θ^*) is:

$$(m^*, n^*, \theta^*) = \arg\max_{m,n,\theta}(a \star b_\theta)_{mn}.$$

In practice we consider a discrete grid of rotations $\boldsymbol{\Theta} \subset [-180°, 180°]$. The registration procedure is outlined in algorithm 1. We refer to the matrix that is rotated as the "target." The result is the estimated registration of the target matrix to the "source" matrix.

Data: Source matrix A, target matrix B, and rotation grid $\boldsymbol{\Theta}$
Result: Estimated registration of B to A, (m^*, n^*, θ^*), and cross-correlation
       function maximum, $CCF_{\max}$
for $\theta \in \boldsymbol{\Theta}$ **do**
   | Rotate B by θ to obtain B_θ;
   | Calculate $CCF_{\max,\theta} = \max_{m,n}(a \star b_\theta)_{mn}$;
   | Calculate translation $[m_\theta^*, n_\theta^*] = \arg\max_{m,n}(a \star b_\theta)_{mn}$
end
Calculate overall maximum correlation $CCF_{\max} = \max_\theta\{CCF_{\max,\theta} : \theta \in \boldsymbol{\Theta}\}$;
Calculate rotation $\theta^* = \arg\max_\theta\{CCF_{\max,\theta} : \theta \in \boldsymbol{\Theta}\}$;
return *Estimated rotation θ^*, translation $m^* = m_{\theta^*}^*$ and $n^* = n_{\theta^*}^*$, and $CCF_{\max}$*
               Algorithm 1: Image Registration Procedure

Handling Missingness

[**Not sure what to do with this section. It needs to be mentioned, but in more or less detail?**]

The registration estimation procedure outline above, namely the Fast Fourier Transform algorithm, does not permit missing values in A or B. It is common for cartridge case scans to contain many missing values - the gray regions in [preprocessing Figure] represent structural values in the scan. Thus, when calculating the CCF we impute these missing values with the average non-missing value in the scan.

We wish to measure the similarity between A and B while taking this missingness into account; to measure the similarity between the non-missing intersection of the aligned scans. We compute the *pairwise-complete correlation* using only the complete value pairs, meaning neither value is missing, between A and B.

Registration-Based Features

Full-Scan Registration   We first estimate the registration between two full scans A and B using algorithm 1 with a rotation grid $\Theta = \{-30°, -27°, ..., 27°, 30°\}$. This results in an estimated registration (m^*, n^*, θ^*) and similarity measure $CCF_{\max}$. We also perform algorithm 1 with the roles of A and B reversed, meaning the target scan A is aligned to source scan B to obtain A^*.

To accommodate these two comparison directions, we introduce a new subscript $d = A, B$, referring to the source scan in algorithm 1. Consequently, we obtain two sets of sets of estimated registrations, $(m_d^*, n_d^*, \theta_d^*)$ and $CCF_{\max,d}$ for $d = A, B$.[2] For $d = A$, we then apply the registration transformation $(m_A^*, n_A^*, \theta_A^*)$ to B to obtain B^* and compute the pairwise-complete correlation, $cor_{\text{full},A}$, between A and B^*. We repeat this in the other comparison direction to obtain $cor_{\text{full},B}$ and average the two:

$$\overline{cor}_{\text{full}} = \frac{1}{2} \left(cor_{A,\text{full}} + cor_{B,\text{full}} \right).$$

We assume that the **average full-scan pairwise-complete correlation** is large for truly matching cartridge cases.

Cell-Based Registration   Following the full-scan registration, we next perform a cell-based registration procedure. [Song (2013)] points out that breech face impressions rarely appear uniformly on a cartridge case surface. Rather, distinguishing markings appear in specific, usually small, regions of a scan (the author refers to these as *valid correlation regions*). Calculating a correlation between two whole scans does not necessarily capture the similarity between these regions. [Song (2013)] proposes partitioning a scan into a rectangular grid of "cells" to isolate the valid correlation regions. Figure 4 shows an example of matrix A partitioned into a grid of 8×8 cells.

---

[2]In reality, the true aligning registrations in the two comparison directions are opposites of each other. However, because we compare discretely-indexed arrays using a nearest-neighbor interpolation scheme, the estimated registrations differ slightly.
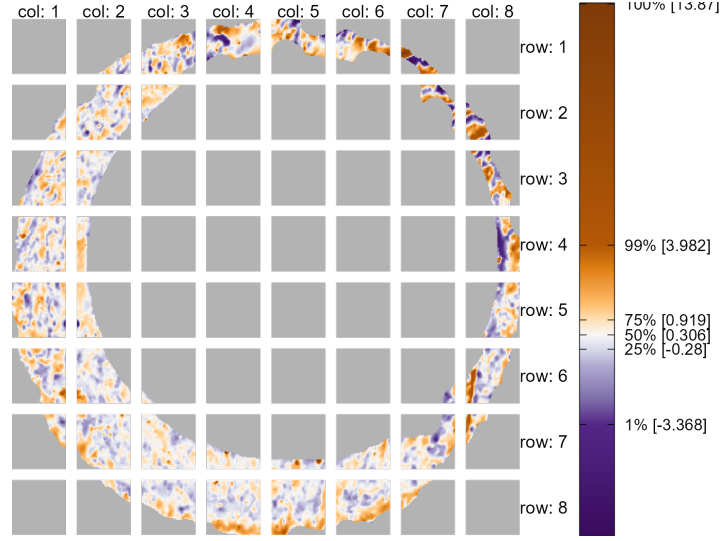
Figure 4: A source scan separated into a grid of 8×8 cells. Each source cell is compared to a target scan to estimate where it aligns best. We exclude cells containing only missing values (visualized here as gray pixels).

The cell-based comparison procedure begins with selecting one of the matrices, say A, as the "source" matrix to be partitioned into a grid of cells. Each of these source cells will be compared to the "target" matrix, in this case B^*. Because A and B^* are already partially aligned based on the course rotation grid $\mathbf{\Theta}$, we compare each source cell to B^* using a new rotation grid of $\mathbf{\Theta}'_A = \{\theta^*_A - 2°, \theta^*_A - 1°, \theta^*_A, \theta^*_A + 1°, \theta^*_A + 2°\}$.

We now extend the surface matrix notation introduced previously to accommodate cells. Let A_t denote the tth cell of matrix A, $t = 1, ..., T_A$ where T_A is the total number of cells containing non-missing values (e.g., $T_A = 38$ in Figure 4) in scan A and let $(a_t)_{ij}$ denote the i, j-th element of A_t.

The cell-based comparison procedure is outlined in algorithm 2.

Data: Source matrix A, target matrix B^*, cell grid size $R \times C$, and rotation grid
$\qquad \mathbf{\Theta}'_A$
Result: Estimated translations and $CCF_{\max}$ values per cell, per rotation
Partition A into a grid of $R \times C$ cells;
Discard cells containing only missing values, leaving T_A remaining cells;
for $\theta \in \mathbf{\Theta}'_A$ **do**
$\quad$ Rotate B^* by θ to obtain B^*_θ;
$\quad$ **for** $t = 1, ..., T_A$ **do**
$\qquad$ Calculate $CCF_{\max,A,t,\theta} = \max_{m,n}(a_t \star b^*_\theta)_{mn}$;
$\qquad$ Calculate translation $[m^*_{A,t,\theta}, n^*_{A,t,\theta}] = \arg\max_{m,n}(a_t \star b^*_\theta)_{mn}$
$\quad$ **end**
end
return $\boldsymbol{F}_A = \{(m^*_{A,t,\theta}, n^*_{A,t,\theta}, CCF_{\max,A,t,\theta}, \theta) : \theta \in \mathbf{\Theta}'_A, t = 1, ..., T_A\}$
Algorithm 2: Cell-Based Comparison Procedure

Rather than exclusively returning the registration that maximizes the overall CCF as in algorithm 1, algorithm 2 returns the set $\boldsymbol{F}_A$ of translations and CCF values for each cell

and each rotation considered. If two cartridge cases are truly matching, then we assume that multiple cells will "agree" on a particular translation value at the true rotation.[3] This agreement phenomenon is illustrated in Figure 5 where each point represents the translation that maximizes the CCF for a particular cell and rotation. The points appear randomly distributed for most of the rotation values except around $\theta = 3$ where a tight cluster of points forms around translation $[17, -16]$. This is evidence to suggest that a true registration exists for these two cartridge cases, implying that they match. The task is to determine when cells reach a registration consensus.
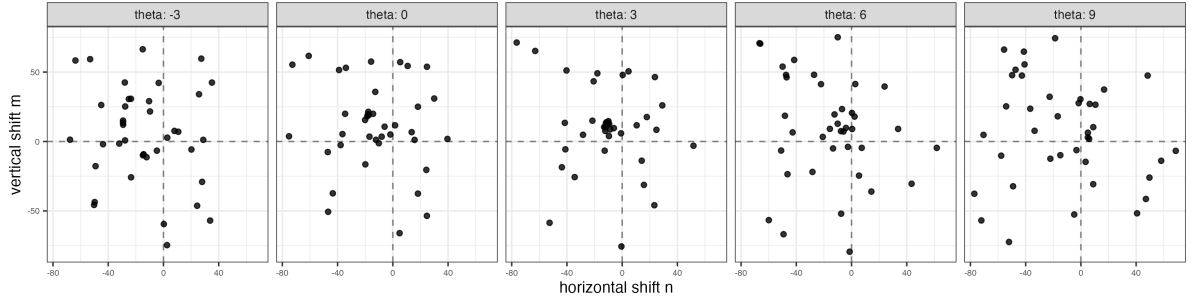

Figure 5: A scatterplot where points represent the cell-wise estimated translations faceted by rotation for a matching pair of cartridge cases. As evidenced by the tight cluster in the middle facet, it appears that multiple cells agree on a translation of $[\hat{m}, \hat{n}] \approx [17, -16]$ after rotating by 3°. Points are jittered for visibility.

Just as with the whole-scan registration, we calculate the pairwise-complete correlation between each cell A_t and a matrix $B_{\theta,t}^*$ of the same size extracted from B_θ^* after translating by $[m_{A,\theta}^*, n_{A,\theta}^*]$. From this we obtain a set of pairwise-complete correlations for each rotation: $\{cor_{A,t,\theta} : \theta \in \mathbf{\Theta}_A'\}$. This whole procedure is repeated using B as the source scan and A^* as the target, resulting in registration set $\mathbf{F}_B$ and pairwise-complete correlations $\{cor_{B,t,\theta} : \theta \in \mathbf{\Theta}_B'\}$.

For $d = A, B$ and $t = 1, ..., T_d$, define the cell-wise maximum CCF and pairwise-complete correlation as:

$$CCF_{\max,d,t} = \max_\theta \{CCF_{\max,d,t,\theta} : \theta \in \mathbf{\Theta}_d'\}$$
$$cor_{d,t} = \max_\theta \{cor_{d,t,\theta} : \theta \in \mathbf{\Theta}_d'\}$$

We compute the following features using the correlation data:

$$\overline{cor}_{\text{cell}} = \frac{1}{T_A + T_B} \sum_{d \in \{A,B\}} \sum_{t=1}^{T_d} cor_{d,t}$$

$$s_{cor}^2 = \frac{1}{T_A + T_B - 1} \sum_{d \in \{A,B\}} \sum_{t=1}^{T_d} (cor_{d,t} - \overline{cor}_{\text{cell}})^2$$

We expect the **average cell-based pairwise-complete correlation** to be large and the **standard deviation of the cell-based pairwise-complete correlations** small for truly matching cartridge case pairs.

---

[3]And that cells will not come to such an agreement for a non-matching pair of cartridge cases

For $d = A, B$ and $t = 1, ..., T_d$, define the per-cell estimated translations and rotation as:

$$\theta_{d,t}^* = \arg\max_{\theta}\{CCF_{\max,d,t,\theta} : \theta \in \mathbf{\Theta}_d'\}$$

$$m_{d,t}^* = m_{\theta_{d,t}^*,d,t}^*$$

$$n_{d,t}^* = n_{\theta_{d,t}^*,d,t}^*$$

We compute the following additional features using the estimated cell translations and rotations:

$$s_{\theta^*}^2 = \frac{1}{T_A + T_B - 1} \sum_{d\in\{A,B\}} \sum_{t=1}^{T_d} (\theta_{d,t}^* - \bar{\theta}^*)^2$$

$$s_{m^*}^2 = \frac{1}{T_A + T_B - 1} \sum_{d\in\{A,B\}} \sum_{t=1}^{T_d} (m_{d,t}^* - \bar{m}^*)^2$$

$$s_{n^*}^2 = \frac{1}{T_A + T_B - 1} \sum_{d\in\{A,B\}} \sum_{t=1}^{T_d} (n_{d,t}^* - \bar{n}^*)^2$$

where

$$\bar{m}^* = \frac{1}{T_A + T_B} \sum_{d\in\{A,B\}} \sum_{t=1}^{T_d} m_{d,t}^*$$

$$\bar{n}^* = \frac{1}{T_A + T_B} \sum_{d\in\{A,B\}} \sum_{t=1}^{T_d} n_{d,t}^*$$

$$\bar{\theta}^* = \frac{1}{T_A + T_B} \sum_{d\in\{A,B\}} \sum_{t=1}^{T_d} \theta_{d,t}^*.$$

We expect the **sample variance of the cell-based estimated registration** values to be small.

From the full-scan and cell-based registration procedures, we obtain six features summarized in Table 1.

Density-Based Features

As discussed in the last section, we wish to identify when multiple cells agree on a particular registration. [Zhang et al. (2020)] proposed using the Density-Based Spatial Clustering of Applications with Noise (DBSCAN) algorithm to identify clusters of points based on their density.

Figure 6 depicts an illustration of the DBSCAN algorithm [cite Wikimedia commons]. XXX get rid of this figure - I'm sure that you can explain the dbscan algorithm as well without giving space to figures that aren't yours. Space is the most valuable resource in a paper :) The algorithm has two parameters: a neighborhood radius ϵ and a minimum point threshold $Minpts$. In Figure 6, $Minpts = 4$ and ϵ is arbitrary and represented by the radius of the circles drawn around each point - each circle represents the ϵ-neighborhood for its center point. First, the algorithm identifies cluster "core"

Notation	Feature Description
$\overline{cor}_{\text{full}}$	**Full-scan pairwise-complete correlation** after aligning the scans.
$\overline{cor}_{\text{cell}}$	**Average cell-based pairwise-complete correlation** after aligning source cells to the target matrix using the cross-correlation function
s^2_{cor}	**Sample variance of the cell-based pairwise-complete correlation** after aligning source cells to the target matrix using the cross-correlation function
s^2_{m*}	**Sample variance of the cell-based vertical translations**
s^2_{n*}	**Sample variance of the cell-based horizontal translations**
$s^2_{\theta*}$	**Sample variance of the cell-based rotations**

Table 1: Six similarity features based on registering full scans or cells.

points that contain at least *Minpts* points within an ϵ distance.[4] These points form the beginning of a cluster and are shown in red in Figure 6. The yellow points B and C are within the ϵ-neighborhood of a core point, but are not themselves core points. They are also included in the cluster making the overall cluster size 8. Finally, the blue point labelled N is not in any core point's ϵ-neighborhood and is thus classified as a "noise point." Unlike other clustering algorithms, the DBSCAN algorithm does not require a specified number of expected clusters as a parameter; any points not belonging to a cluster are "noise."
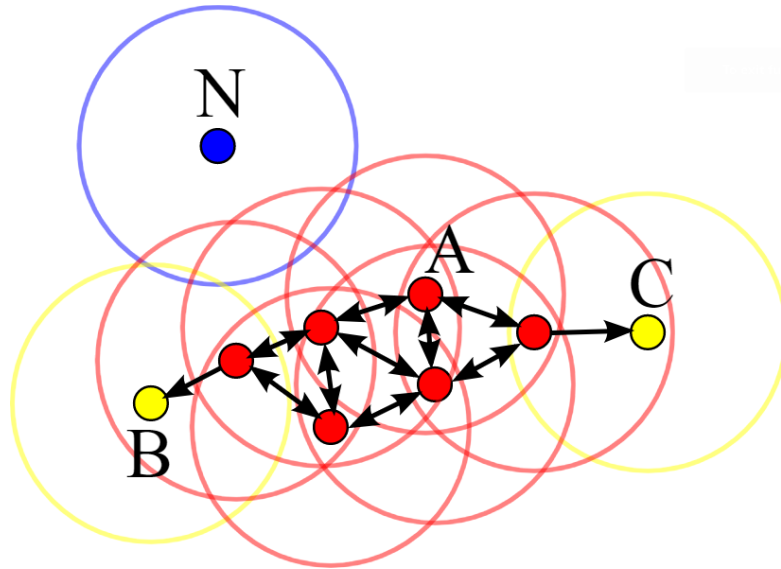

Figure 6: Illustration of the DBSCAN algorithm [cite]. Red and yellow points are part of the same cluster with the former forming the "core" of the cluster. The blue point is not part of a cluster and is classified as a "noise point." Figure by Chire - Own work, CC BY-SA 3.0, https://commons.wikimedia.org/w/index.php?curid=17045963

---

[4]Euclidean distance, in our application

Figure 7 shows an example of DBSCAN cluster assignments for the known-match pair A and B shown in Figure 3. The left scatterplot shows the per-cell estimated translations $[m^*_{d,t,\theta}, n^*_{d,t,\theta}]$ for $\theta = 3°$ when scan A is used as source and B^* as target, resulting a cluster of size 14. The right scatterplot shows the per-cell estimated translations with the roles of A and B^* reversed: now B^* is partitioned into a grid of source cells that are compared to A, resulting in a cluster of size 13.
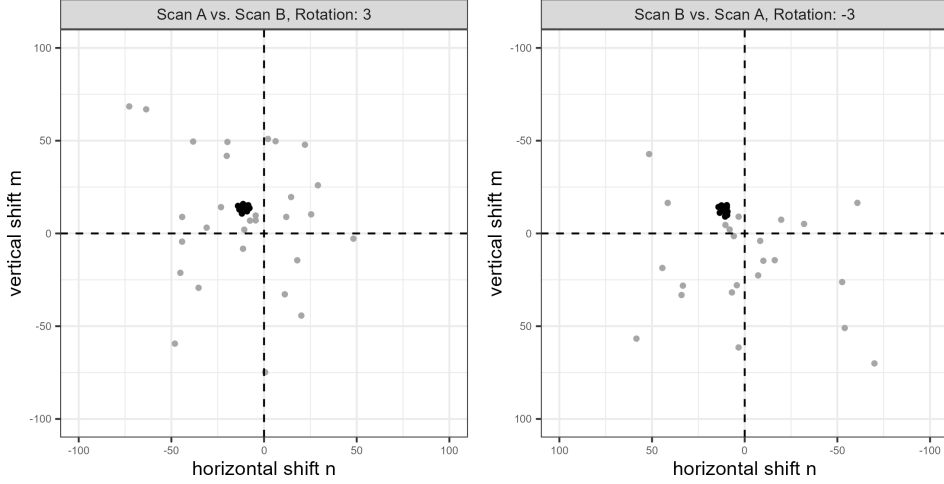

Figure 7:   Cluster assignments based on the Density Based Spatial Clustering with Applications to Noise (DBSCAN) algorithm for estimated translations in two comparison directions. Using scan A as source results in a cluster of size 14 (left) compared to 13 when scan B is used as source (right). Noting the reversed axes in the right plot, we see that the clusters are located approximately opposite of each other. Points are jittered for visibility.

Because A and B are truly matching, we expect the estimated registrations in these two comparison directions to be opposites. Indeed, the mean cluster centers in Figure 7 are $(\hat{m}_A, \hat{n}_A, \hat{\theta}_A) \approx (16.9, -16.7, 3°)$ when A is used as source compared to $(\hat{m}_B, \hat{n}_B, \hat{\theta}_B) \approx (-16.2, 16.8, -3°)$ when B^* is used as source.

We calculate numerical features based on the DBSCAN cluster assignments. We first use a 2D kernel density estimator [cite kde2d from MASS(?)] to identify the rotation $\hat{\theta}_d$ at which the per-cell translations achieve the highest density. Next, we compute clusters using the DBSCAN algorithm amongst the estimated translations $\{(m^*_{d,t,\hat{\theta}_d}, n^*_{d,t,\hat{\theta}_d}) : t = 1, ..., T_d\}$ like those shown in Figure 7.[5] Let $\boldsymbol{C}_d$ denote the set of cells in the DBSCAN cluster. We treat the mean cluster centers as the estimated translations $[\hat{m}_d, \hat{n}_d]$.

We consider features related to whether a DBSCAN cluster is identified in both comparison directions and, if such clusters are identified, the average size of the clusters. We also compare the density-estimated rotations and translations across the two com-

---

[5]If more than one cluster is identified, we binarize the points based on whether they were assigned to any cluster or if they are a noise point and proceed as if there is only one cluster. We assume that two or more clusters form only because of the course rotation grid considered. Were a finer grid used, the points would coalesce into a single cluster around the true translation value. This assumption has empirical support through our experimentation.

parison directions. These are summarized in the following features:

$$C = \frac{1}{2} \left(|\boldsymbol{C}_A| + |\boldsymbol{C}_B| \right)$$
$$C_0 = I(|\boldsymbol{C}_A| > 0 \text{ and } |\boldsymbol{C}_B| > 0)$$
$$\Delta_\theta = |\hat{\theta}_A + \hat{\theta}_B|$$
$$\Delta_{trans} = \sqrt{(\hat{m}_A + \hat{m}_B)^2 + (\hat{n}_A + \hat{n}_B)^2}$$

where $|\boldsymbol{C}_d|$ denotes the cardinality of $\boldsymbol{C}_d$ and $I(\cdot)$ is the identify function equals 1 if the predicate argument "·" evaluates to TRUE and 0 otherwise. We use both C and C_0 because of potential missingness in the values of C if no cluster is identified. Missing C values are imputed using the median non-missing value when fitting classifiers, so the missingness information is retained in C_0.

For truly matching cartridge case pairs, we expect the **average DBSCAN cluster size** to be large, the DBSCAN **cluster indicator** to be 1, and the **difference in the density-estimated registrations** to be small.

From this DBSCAN procedure, we obtain four features summarized in Table 2.

Notation	Feature Description
C	**Average DBSCAN cluster size** across both comparison directions
C_0	**Cluster indicator** variable indicating the existence of DBSCAN clusters in both comparison directions
Δ_θ	**Absolute sum of the density-estimated rotations** between both comparison directions
Δ_{trans}	**Root sum of squares of the cluster-estimated translations** between both comparison directions

Table 2: Three similarity features based on the density-based clustering procedure.

Visual Diagnostic Features

The final set of features we calculate are based on visual diagnostic tools described in [Zemmels et al. (2023)]. These numerical features quantify the qualitative observations one can make from the diagnostics.

To create the visual diagnostics, we perform element-wise matrix operations. In particular, for a matrix $X \in \mathbb{R}^{k \times k}$ and condition $cond : \mathbb{R}^{k \times k} \to \{TRUE, FALSE\}^{k \times k}$, we define an element-wise filter operation $\mathcal{F} : \mathbb{R}^{k \times k} \to \mathbb{R}^{k \times k}$ as:

$$\mathcal{F}_{cond}(X) = (f_{ij})_{1 \leq i,j \leq k} = \begin{cases} x_{ij} & \text{if } cond \text{ is } TRUE \text{ for element } i,j \\ NA & \text{otherwise} \end{cases}$$

Of particular interest in our application is the (absolute) difference between surface matrices. For example, $\mathcal{F}_{|A-B|>\tau}(A)$ contains elements of matrix A where the pair of scans A and B deviate by at least $\tau \in \mathbb{R}$. Surface values in A and B^* that are "close," meaning within τ distance, to each other are replaced with NA in this filtered matrix.

The Complementary Comparison Plot visualizes the similarities and differences between two scans. Figure 8 shows a Complementary Comparison plot between scan A and B^* defined previously. The left column shows Scans A and B^*. The middle column shows a filtered element-wise average between A and B^*; namely $\mathcal{F}_{|A-B^*|<\tau}\left(\frac{1}{2}(A+B^*)\right)$. This filtered element-wise average emphasizes similarities between A and B^*. The right column shows $\mathcal{F}_{|A-B^*|>\tau}(A)$ and $\mathcal{F}_{|A-B^*|>\tau}(B^*)$ on top and bottom, respectively. These plots emphasize the differences between the two scans. The complementary comparison plot is a powerful tool for assessing the estimated alignment and identifying similarities and differences between two surface matrices. We repeat this in the other comparison direction $(d = B)$ to obtain filtered matrices $\mathcal{F}_{|A^*-B|<\tau}\left(\frac{1}{2}(A^*+B)\right)$, $\mathcal{F}_{|A^*-B|>\tau}(A^*)$ and $\mathcal{F}_{|A^*-B|>\tau}(B)$.[6]
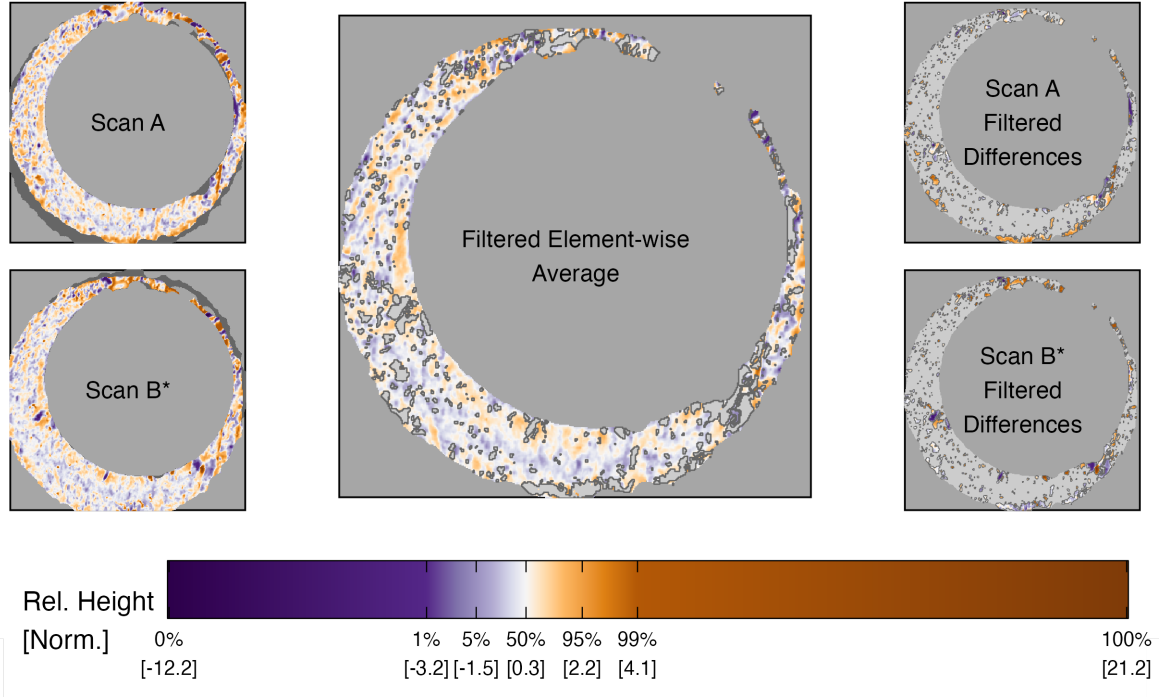

Figure 8:   Full scan comparison plot.

We make a series of qualitative assumptions related to how a Complementary Comparison Plot will look for matching and non-matching cartridge case pairs. We develop a set of features that measure the degree to which these assumptions are met by a particular cartridge case pair. We now describe each feature and their associated assumptions.

We first consider the correlation $cor_{d,\text{full,filt}}$ between the filtered matrices $\mathcal{F}_{|A-B^*|>\tau}(A)$ and $\mathcal{F}_{|A-B^*|>\tau}(B^*)$ when $d = A$ and $\mathcal{F}_{|A^*-B|>\tau}(A^*)$ and $\mathcal{F}_{|A^*-B|>\tau}(B)$ when $d = B$. The average of these is used as a feature:

$$\overline{cor}_{\text{full,filt}} = \frac{1}{2}\left(cor_{A,\text{full,filt}} + cor_{B,\text{full,filt}}\right).$$

---

[6]As with the registration-based features, in reality these matrices should be equivalent across the two comparison directions. However, there are slight differences due to the discretely-indexed nature of the surface matrices.

We assume that **average filtered full-scan pairwise-complete correlation** will be larger for truly matching A and B than non-matching. Said another way, we assume that even surface regions of A and B that are different will follow similar trends, which can occur due to variability in the amount of contact between a cartridge case and breech face across multiple fires of a single firearm. The correlation is calculated by vectorizing the two filtered surface matrices and treating missing values by case-wise deletion.

As before, we extend this notation to accommodate cell comparisons $t = 1, ..., T_d$ for $d = A, B$ using subscripts: $cor_{d,t,\text{filt}}$. For example, $cor_{A,t,\text{filt}}$ is the correlation between cell filtered surface matrices $\mathcal{F}_{|A_t - B^*_{t,\theta^*_t}| > \tau}(A_t)$ and $\mathcal{F}_{|A_t - B^*_{t,\theta^*_t}| > \tau}(B^*_{t,\theta^*_t})$ where B^*_{t,θ^*_t} is the matrix extracted from B^* that maximizes the CCF with A_t. We calculate the sample mean of the filtered correlation values across all cells and both directions:

$$\overline{cor}_{\text{cell,filt}} = \frac{1}{T_A + T_B} \sum_{d \in \{A,B\}} \sum_{t=1}^{T_d} cor_{d,t,\text{filt}}$$

Next, we consider features based on the elements of the Boolean *cond* matrix. Consider Figure 9 that shows the filtered element-wise average $\mathcal{F}_{|A-B^*| < \tau}\left(\frac{1}{2}(A + B^*)\right)$ on the left and the associated *cond* matrix $|A - B^*| < \tau$ visualized in black-and-white in the middle where filtered elements are shown in white. We use a connected components labeling algorithm detailed in [Haralick and Shapiro (1992)] to identify individual neighborhoods of filtered elements. More precisely, the algorithm returns a set of sets $\boldsymbol{S}_d = \{S_{d,1}, S_{d,2}, ..., S_{d,L_d}\}$ where each $S_{d,l}$ is a set of indices of the *cond* matrix that have a value of $TRUE$ and are connected by a chained-together sequence of 4 (Rook's) neighborhoods. The right side of Figure 9 shows each $S_{d,l}$ distinguished by different fill colors, $l = 1, ..., L_d$.
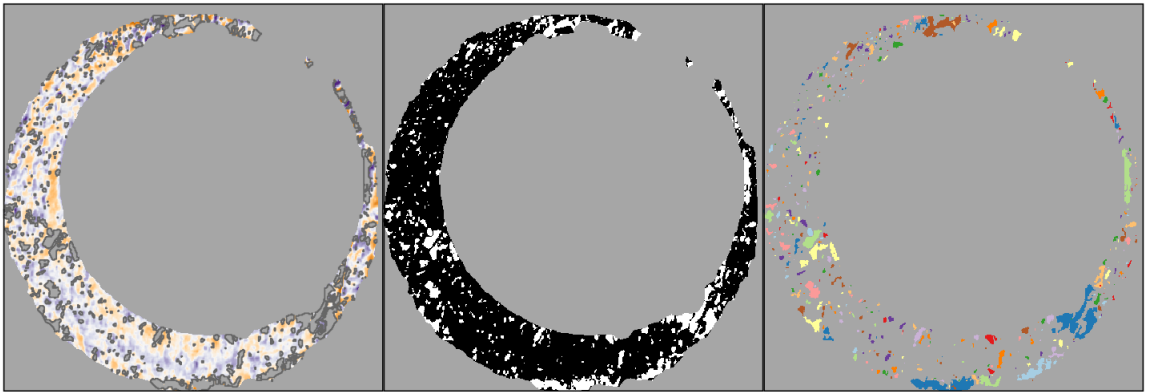

Figure 9: (Left) After aligning two scans, we filter regions that are "different" from each other, meaning the absolute difference between surface values is larger than some threshold. (Middle) We binarize the scan into "filtered" or "non-filtered" regions - shown in white and black, respectively. (Right) Using a connected components labeling algorithm, we identify connected "neighborhoods" of filtered elements. We assume that these neighborhoods will be small, on average, if comparing truly matching cartridge cases.

We calculate the following features using the full-scan labeled neighborhoods:

$$\overline{|S|}_{\text{full}} = \frac{1}{L_A + L_B} \sum_{d \in \{A,B\}} \sum_{l=1}^{L_d} |S_{d,l}|$$

$$s^2_{\text{full},|S|} = \frac{1}{L_A + L_B - 1} \sum_{d \in \{A,B\}} \sum_{l=1}^{L_d} (|S_{d,l}| - \overline{|S|}_{\text{full}})^2$$

where $|S_{d,l}|$ is the size of the set $S_{d,l}$. We assume that the **average** and **sample variance of the filtered full-scan neighborhood sizes** will be small for truly matching cartridge cases. That is to say, we assume that the the surface regions of A and B that are different will all be small, on average, and vary little in size. This assumption is appropriate assuming that the breech face leaves consistent markings on fired cartridge cases.

Again, we extend the notation to accommodate individual cells. Let $\boldsymbol{S}_{d,t} = \{S_{d,t,1}, ..., S_{d,t,L_{d,t}}\}$ denote the set of labeled neighborhoods for a cell $t = 1, ..., T_d$, $d = A, B$. We calculate the per-cell average and sample variance of the labeled neighborhood cell size:

$$\overline{|S|}_{d,t} = \frac{1}{L_{d,t}} \sum_{l=1}^{L} |S_{d,t,l}|$$

$$s^2_{d,t,|S|} = \frac{1}{L_{d,t} - 1} \sum_{l=1}^{L_{d,t}} (|S_{d,t,l}| - \overline{|S|}_{\text{cell},d,t})^2.$$

We assume that the cell-based $\overline{|S|}_{d,t}$ and $s^2_{d,t,|S|}$ will be small, on average, for truly matching cartridge cases. Consequently, we use the sample average of these as features:

$$\overline{|S|}_{\text{cell}} = \frac{1}{T_A + T_B} \sum_{d \in \{A,B\}} \sum_{t=1}^{T_d} \overline{|S|}_{d,t}$$

$$\bar{s}^2_{\text{cell},|S|} = \frac{1}{T_A + T_B} \sum_{d \in \{A,B\}} \sum_{t=1}^{T_d} s^2_{d,t,|S|}$$

Again, we assume that the **average cell-wise neighborhood size** and the **average sample variance of the cell-wise neighborhood sizes** will be small for truly matching cartridge cases.

Table 3 summarizes the 7 features calculated based on the visual diagnostics.

4.3. Scoring

We randomly split the cartridge case data set into 10 barrels for training and 15 barrels for testing. Multiple cartridge cases were fired from each barrel, so this resulted in a training data set of 210 cartridge cases, $\binom{210}{2} = 21,945$ pairwise comparisons, and a testing set of 300 cartridge cases, $\binom{300}{2} = 44,850$ pairwise comparisons.

We perform 10-fold cross-validation to train binary classifiers. We compare the results of three classifiers: based on a logistic regression, a classification tree Therneau and Atkinson (2022), and a random forest (Liaw and Wiener 2002; Breiman 2001). We make use of the testing/training infrastructure of the **caret** package Kuhn (2022).

Notation	Feature Description
$\overline{cor}_{\text{full,filt}}$	**Average filtered full-scan correlation** across both comparison directions
$\overline{cor}_{\text{cell,filt}}$	**Average filtered cell-wise correlation** across all cells in both comparison directions
$\overline{|S|}_{\text{full}}$	**Average filtered full-scan neighborhood size** across both comparison directions
$s^2_{\text{full},|S|}$	**Sample variance of the filtered full-scan neighborhood sizes** across both comparison directions
$\overline{|S|}_{\text{cell}}$	**Average filtered cell-wise neighborhood sizes** across all cells in both comparison directions
$\bar{s}^2_{\text{cell},|S|}$	**Average sample variance of the cell-wise neighborhood sizes** across all cells in both comparison direction

Table 3: Seven similarity features calculated based on visual diagnostics.

[Write full logistic regression model here]

We consider the pros and cons of each of these models. The logistic regression and CART models are more interpretable than a random forest yet, as we will see, a random forest tends to be more accurate. The following section detail the results of this cross-validation procedure.

5. Results

5.1. Training Results

Figure 10 shows the cross-validation estimated accuracies for the three trained models. We consider the performance of the three models under different subsets of the overall data, which provides insight into the importance of the various feature groups. We see that the random forest trained on the full ACES data set results in the highest overall accuracy of 98.9%. For each feature group, the the random forest yields the highest accuracy followed by the logistic regression and CART models. We see that the removing the cluster-based features has a notable impact on the accuracy of the logistic regression and CART models, while the random forest is more is more robust.

Figure 12 shows the distribution of a variable importance measure for each feature across fittings of a random forest model using 10 random seeds. For each replicate, we measure a variable's importance using the Gini Index, which measures the probability of making a misclassification for a given model [cite Gini Index resource]. [More exposition on Gini Index?] Noting the log scale on which these points are plotted, we see that the "no cluster indicator" variable is considered by far the most important variable across the random forest fittings. The "cell-based pairwise-complete correlation" and "cluster size" are also important, although it's less clear which is more important due to their distributional overlap. Overall, the results indicate that the cluster-based aggregation and cell-based registration features are considered most important by the random forest models.
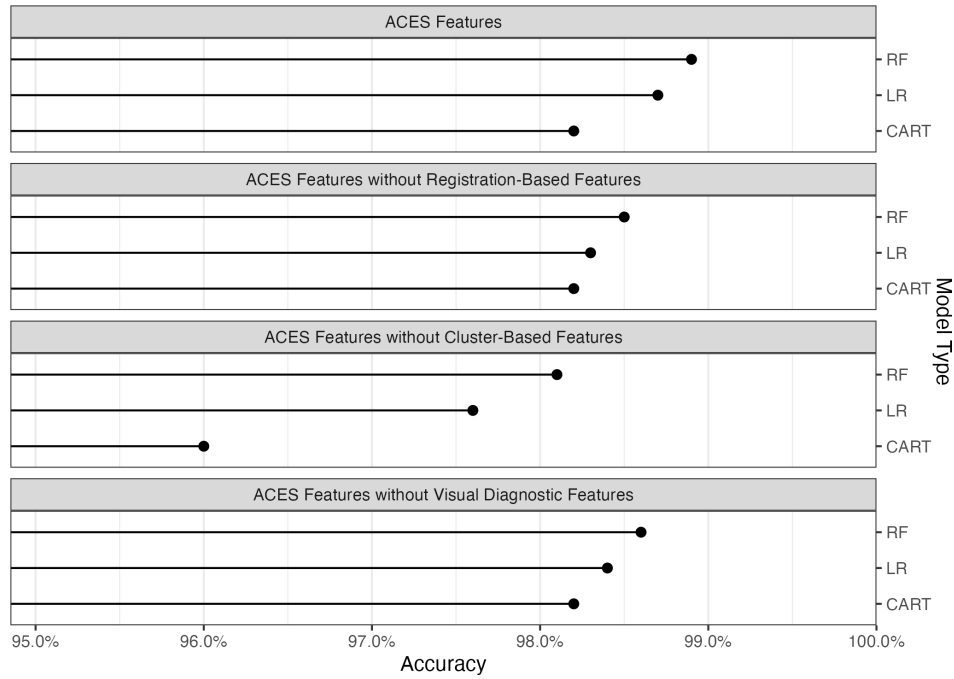
Figure 10:   Training classification accuracy for random forest (RF), logistic regression (LR), and classification and regression tree (CART) models based on various subsets of the training data set features. These accuracies are estimated based on 10-fold cross validation repeated thrice. In general, the Classification and Regression Tree (CART) model performs poorest while the Random Forest performs best. Removing the cluster-based features has the largest impact on the accuracies.
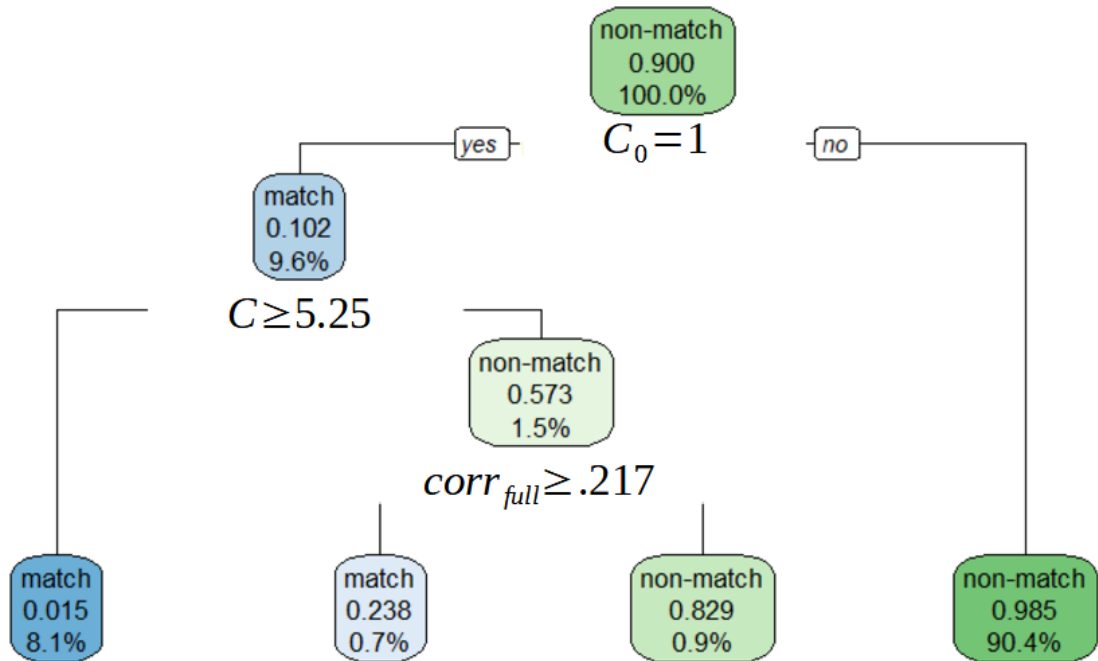

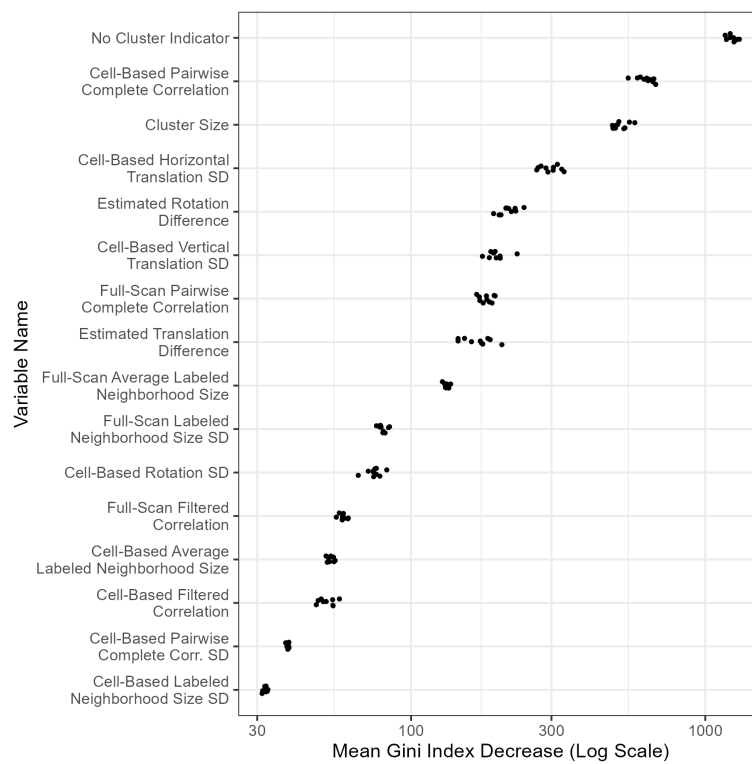Figure 11:   Trained Classification and Regression Tree model.

Figure 12: Variable importance measures from fitting a random forest to the training data set, repeated 10 times under various random seeds. Points are plotted on a log scale and vertically jittered for visibility. The No Cluster Indicator feature is by far the most important feature, as measured by the mean decrease in the Gini index.
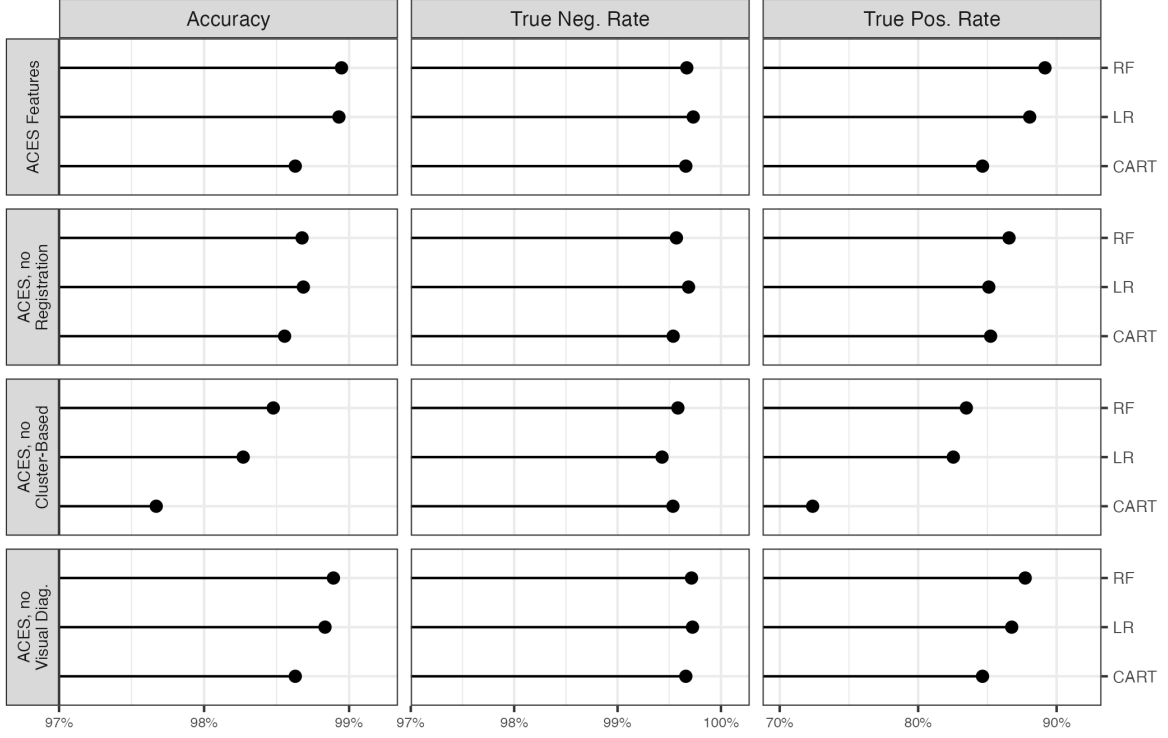
Figure 13:   Testing classification accuracy, false negative rate, and false positive rate faceted by various subsets of the testing data set features. The Logistic Regression model performs about as well as the Random Forest model in classifying matches and non-matches amongst the test data set. This is primarily because the Logistic Regression model is has a higher true negative rate. In contrast, the Random Forest model has a higher true positive rate. The CART model lags behind in the three metrics, particularly when the cluster-based features are omitted from the data set.

5.2. Testing Results

For each of the 44,850 cartridge case pairs in the testing data set, we use each model to predict whether the pair is a match or non-match. An error occurs when this prediction does not match the ground-truth nature of the cartridge case pair. Figure 13 summarizes the error rates for each method. The Accuracy is the overall percentage of correct classifications. The True Negative rate is percentage of correctly-classified non-match pairs. Conversely, the True Positive rate is the percentage of correctly-classified matching pairs.

We see that the testing accuracy across models and feature groups is similar to that of the training results in Figure 10. The random forest is more robust to changes in feature group while the CART model performs uniformly worse than the other models. Interestingly, the logistic regression model performs slightly better than the random forest for some feature groups. Considering the true positive and negative rates, this can be explained by the specificity of the models: the logistic regression model classifies non-matches more effectively in these instances, although this difference is slight.

6. Discussion

[Discuss importance of various feature groups] [Zhang et al. (2020)] proposed a binary classifier using the DBSCAN algorithm: if a cluster is identified, then classify the cartridge case pair as a match and otherwise a non-match. We treat the existence of clusters, along with the size of of those clusters, as features for a classifier.

Our intention in fitting different classification models was to compare each model's strengths and weaknesses. As observed previously, the random forest has the overall best accuracy out of the three models with the logistic regression classifier being a consistent close second. In particular, the random forest model is better at identifying truly matching cartridge cases than the logistic regression classifier, yet worse at identifying non-matches.

Pragmatically, it seems reasonable to choose the model with the highest estimated accuracy. Ethically, we might favor the model that makes the fewest false positive classifications since mis-classifying a truly non-matching cartridge case pair may incriminate an innocent individual. While the input of statisticians is important, this decision needs to be weighed by the wider forensic and legal communities.

While the random forest is generally more accurate, the CART and logistic regression models are more interpretable. For example, as seen in [figure], the CART model provides a set of simple, binary rules by which we can arrive at a classification. [More on CART? Perhaps compare a single decision tree to random forest?]

The estimated coefficients in the logistic regression model help us understand the effect that each feature has on the odds that a cartridge case pair matches. [Table] shows the multiplicative change in the odds that a cartridge case pair matches for a one unit increase in each feature.

Discuss benefits of three models here

- CART model is a clear set of binary "rules" that lead to a classification

- Logistic Regression provides estimate of how odds of match change with a one unit increase of each feature

    - It also performs similar to the random forest

- Random Forest seems to be more robust to changes

Compare results to best CMC method (and Baldwin?). Qualify that this *our* implementation of the CMC method

7. Conclusion

More experimentation is needed. It is reasonable to assume that the version of ACES discussed in this paper would be effective at classifying cartridge cases of the same brand, fired from the same make/model of firearm, and scanned using the same topographical scanner [cite TopMatch]. It remains to be seen whether the fitted models generalize to other types of ammunition or firearm.

The train/test procedure outlined in this manuscript should be adopted by any future researchers to validate proposed methods. [Discuss availability of data and code]

Nonetheless, this paper provides the largest study of automatic cartridge case comparison algorithms published to-date. Our results indicate that there exist effective, robust, and interpretable automatic classifiers for cartridge case evidence.

We expect the ACES feature set to evolve over time; for discriminatory features to replace less informative features. We stress interpretability as a guiding principle for future feature engineering. Ideally, forensic practitioners will eventually use such algorithms to supplement their expert opinion. We believe it paramount that practitioners understand and can explain, at least at a high level, to a jury of lay people the features used for classification. [More on why this is important]

Computational Details

If necessary or useful, information about certain computational details such as version numbers, operating systems, or compilers could be included in an unnumbered section. Also, auxiliary packages (say, for visualizations, maps, tables, . . .) that are not cited in the main text can be credited here.

The results in this paper were obtained using R~3.5.1. I think this version of R is outdated :) R Core Team (2019) R itself and all packages used are available from the Comprehensive R Archive Network (CRAN) at `https://CRAN.R-project.org/`.

acknowledge knitr, the tidyverse, RStudio IDE

Acknowledgments

All acknowledgments should be collected in this unnumbered section before the references. It may contain the usual information about funding and feedback from colleagues/reviewers/etc. Furthermore, information such as relative contributions of the authors may be added here (if any).

XXX CSAFE funding text

References

Baldwin, D. P., Bajic, S. J., Morris, M., and Zamzow, D. (2014). A Study of False-Positive and False-Negative Error Rates in Cartridge Case Comparisons. Technical report, Ames Lab IA, Performing, Fort Belvoir, VA, DOI: `10.21236/ADA611807`.

Breiman, L. (2001). Random Forests. *Machine Learning*, 45(1):5–32, DOI: `10.1023/a:1010933404324`, `http://dx.doi.org/10.1023/A:1010933404324`.

Ester, M., Kriegel, H.-P., Sander, J., and Xu, X. (1996). A density-based algorithm for discovering clusters in large spatial databases with noise. In *Proceedings of the Second International Conference on Knowledge Discovery and Data Mining*, KDD'96, page 226–231. AAAI Press.

Hare, E., Hofmann, H., and Carriquiry, A. (2017). Automatic matching of bullet land impressions. *The Annals of Applied Statistics*, 11(4):2332–2356, ISSN: `19326157`, `http://www.jstor.org/stable/26362188`.

Hofmann, H., Vanderplas, S., Krishnan, G., and Hare, E. (2022). *x3ptools: Tools for Working with 3D Surface Measurements*, `https://github.com/heike/x3ptools`. R package version 0.0.3.9000.

Kuhn, M. (2022). *caret: Classification and Regression Training*, `https://CRAN.R-project.org/package=caret`. R package version 6.0-91.

Liaw, A. and Wiener, M. (2002). Classification and regression by randomforest. *R News*, 2(3):18–22, `https://CRAN.R-project.org/doc/Rnews/`.

National Research Council (2009). *Strengthening forensic science in the United States: a path forward.* The National Academies Press, Washington, D.C.

PCAST, P. (2016). Forensic science in criminal courts: Ensuring scientific validity of feature-comparison methods. Technical report, Executive Office of The President's Council of Advisors on Science and Technology, Washington DC.

R Core Team (2019). *R: A Language and Environment for Statistical Computing.* R Foundation for Statistical Computing, Vienna, Austria, `https://www.R-project.org/`.

Swofford, H. and Champod, C. (2021). Implementation of algorithms in pattern & impression evidence: A responsible and practical roadmap. *Forensic Science International: Synergy*, 3:100142, DOI: `10.1016/j.fsisyn.2021.100142`, `http://dx.doi.org/10.1016/j.fsisyn.2021.100142`.

Therneau, T. and Atkinson, B. (2022). *rpart: Recursive Partitioning and Regression Trees*, `https://CRAN.R-project.org/package=rpart`. R package version 4.1.16.

Zemmels, J., Hofmann, H., and VanderPlas, S. (2022). *cmcR: An Implementation of the 'Congruent Matching Cells' Method.* R package version 0.1.9.

Affiliation:

Joseph Zemmels
Iowa State University
Center for Statistics and Applications in Forensic Evidence
Iowa State University
195 Durham Center
613 Morrill Road
Ames, IA 50011
E-mail: jzemmels@iastate.edu
URL: https:::/jzemmels.github.io

Susan VanderPlas
University of Nebraska - Lincoln
Department of Statistics
University of Nebraska - Lincoln
343D Hardin Hall
3310 Holdrege St
Lincoln, NE 68588
E-mail: susan.vanderplas@unl.edu
URL: https://srvanderplas.netlify.app/

Heike Hofmann
Iowa State University
Center for Statistics and Applications in Forensic Evidence
Iowa State University
195 Durham Center
613 Morrill Road
Ames, IA 50011
E-mail: heike@iastate.edu
URL: https://github.com/heike